


## Article

# High Temperature Oxidation of Enamel Coated Low-Alloyed Steel 16Mo3 in Water Vapor

Germain Boissonnet <sup>1</sup>, Ewa Rząd <sup>2</sup>, Romain Troncy <sup>1</sup>, Tomasz Dudziak <sup>2</sup> and Fernando Pedraza <sup>1,\*</sup>

<sup>1</sup> Laboratoire des Sciences de l'Ingénieur pour l'Environnement, Université de La Rochelle LaSIE, UMR-CNRS 7356, Avenue Michel Crépeau, CEDEX 1, 17042 La Rochelle, France

<sup>2</sup> Centre for Corrosion Studies, Łukasiewicz Research Network—Krakow Institute of Technology, 73 Zakopiańska St., 30-418 Krakow, Poland

\* Correspondence: fpedraza@univ-lr.fr

**Abstract:** New types of ceramic coatings based on SiO<sub>2</sub>-Na<sub>2</sub>O-B<sub>2</sub>O<sub>3</sub>-TiO<sub>2</sub> oxide phases were investigated as protection for boiler steel in power generation systems. Low-alloyed Cr-Mo 16Mo3 steel was coated with different compositions of enamel coatings to assess the protective potential of these coatings under water vapor at high temperatures. Oxidation at 650 °C for 50 h in Ar + water vapor was performed in a TGA apparatus to investigate the oxidation kinetics. The results indicate that the ceramic coatings provided a high degree of protection for the steel exposed to such conditions compared to the uncoated 16Mo3 steel. Furthermore, despite the formation of cracks in the coatings, no spallation from the steel surface was observed. Interconnected porosity in the coatings is suspected to provoke interfacial degradation.

**Keywords:** ceramic coatings; 16Mo3 steel; high temperature oxidation; TGA; water vapor



**Citation:** Boissonnet, G.; Rząd, E.; Troncy, R.; Dudziak, T.; Pedraza, F. High Temperature Oxidation of Enamel Coated Low-Alloyed Steel 16Mo3 in Water Vapor. *Coatings* **2023**, *13*, 342. <https://doi.org/10.3390/coatings13020342>

Academic Editors: Matic Jovičević-Klug, Patricia Jovičević-Klug and László Tóth

Received: 28 December 2022

Revised: 29 January 2023

Accepted: 30 January 2023

Published: 2 February 2023



**Copyright:** © 2023 by the authors. Licensee MDPI, Basel, Switzerland. This article is an open access article distributed under the terms and conditions of the Creative Commons Attribution (CC BY) license (<https://creativecommons.org/licenses/by/4.0/>).

## 1. Introduction

Energy consumption increases yearly due to the high demand for electricity worldwide; therefore, new systems for the high-temperature protection of structural steels employed in the energy sector must be developed. However, the operating conditions in different plants are particularly aggressive, and different types of corrosion at high temperatures occur. For instance, in most thermal plants, molten sulfate and chloride derivative salts appear that markedly attack the low Cr-containing steel grades, as demonstrated by Abu-warda et al. [1]. Similarly, an extensive sulfidation attack has been recently reported in the typical 16Mo3 boiler steel [2]. Since the use of noble materials is not economically interesting, many various coatings have been proposed in the open literature whether to fight against steam or fireside corrosion. Amongst the former, Al and Al/Si slurry diffusion coatings were demonstrated to withstand long exposures of 100% steam [3] even at high pressures and long exposures [4]. However, such diffusion coatings are relatively brittle and tensile cracks may appear under high pressures allowing steam to penetrate into the substrate material. In addition, the potential interdiffusion of the substrate and coating elements may lower their use for extended periods of time.

The fight against fireside corrosion (and erosion) is mostly conducted through various derivate techniques of thermal spray to produce overlay coatings on the different metal alloys (steels and nickel-based alloys) as reported in the comprehensive reviews of Dhand et al. [5] and of Kumara and collab. [6]. In low-alloy steels, such as 16Mo3, T21, T22 and the alike, various studies have focused on different coating alternatives. For instance, Galetz et al. focused on the use of cladding, self-fluxing, flame spray, and high velocity oxy-fuel (HVOF) to improve the resistance against molten salts of various low-alloy steels [7]. It was concluded that the introduction of Mo and Si in the coatings was beneficial, yet the most protective coatings were those with the lowest porosity and the thickest ones, i.e., the overlay welded alloys and the self-fluxing spray coatings were the most promising

despite their greater cost against the flame-sprayed or HVOF coatings. Jafari and collab. [8] employed high-velocity air–fuel (HVOF) on 16Mo3 boiler steel against KCl-induced hot corrosion in air. When compared with more noble materials (AISI 304 and Sanicro25), the authors found a better performance of the Ni–Al coatings than the Ni–Cr-based ones because the alumina scale grown in the former was denser than the chromia one formed in the latter. This impeded the diffusion of the aggressive chlorine species. Indeed, the chlorides have been reported to induce a great attack on the chromia, also forming NiCr coatings when produced by HVOF [1].

In essence, such thermal spray coating systems show some degree of porosity, depending on the technology used, where ashes can accumulate and initiate accelerated degradation processes of boiler tubes [9,10]. To overcome the problem, new systems based on ceramic compounds are being developed for the high-temperature protection of boiler steels. One of the very first works related to ceramic coatings for steels to be used at a high-temperature regime was presented by Harrison et al. [11]. The coatings were designed for use at temperatures as high as 670 °C while displaying outstanding properties such as high resistance to chipping under repeated thermal shock and protection of the metal against oxidation during prolonged exposures. These 70- $\mu\text{m}$  thick coatings were prepared using a mixture of a special grade of calcined aluminum oxide with a conventional type of ground-coat frit in water that is applied to the steel surface before drying and firing according to well-known methods in the ceramic industry. The development of ceramic coatings for high-temperature applications accelerated since the '70s due to the development of deposition techniques [12]. In 1980, ceramic coatings were applied to adiabatic engines [13]. First, ceramic coatings were employed in gas turbine blades and then in pistons, cylinder linings, valves, and piston crown surfaces [14]. For such applications, ceramic coatings are mainly used for the protection of the base alloys against hot corrosion, oxidation, and wear degradation. One of the most advanced ceramic coatings produced recently are the coatings reducing the based metal temperature (Ni-based superalloys), known as the Thermal Barrier Coatings (TBCs) [15]. Those types of coatings are used in aero-jet engines, as well as in gas turbine technologies [16,17]. The state-of-the-art TBCs are generally based on yttria-stabilized zirconia (YSZ) deposited by Electron Beam Physical Vapor Deposition (EB-PVD) or APS process [18,19]. As a decent alternative, mullite can replace zirconia as a TBC for high-temperature gradient fields [20]. In the energy sector, where temperatures are much lower and the surface area is much larger than in aero jet engines, the gas atmosphere is incomparably worse, and hence, different and cheaper solutions are required. Generally, carbides like silicon carbide (SiC) and tungsten carbide (WC) are used as dispersoids when the hardness and wear resistance of the coatings on boiler tubes against fireside corrosion are the major requirements. Nevertheless, oxides such as  $\text{TiO}_2$ ,  $\text{SiO}_2$ ,  $\text{Al}_2\text{O}_3$ , etc., are used when resistance to hot corrosion and oxidation at high temperatures is required [21]. Therefore, to get a better understanding of advanced ceramic materials for further development in particular engineering applications, e.g., the energy sector and boiler protection, extensive research is essential for evaluating the microstructural and corrosion resistance properties of such coatings. Therefore, this research investigates the oxidation resistance at high temperatures and in the presence of water vapor of new ceramic enamel coatings based on  $\text{SiO}_2$ - $\text{Na}_2\text{O}$ - $\text{B}_2\text{O}_3$ - $\text{TiO}_2$  oxide phases that are applied on low-alloyed 16Mo3 steel.

## 2. Experimental Method

### 2.1. Materials and Coatings

The 16Mo3 steel (0.12 C, 0.4 Mn, <0.35 Si, 0.025 S, 0.025 P, 0.3 Cr, 0.3 Mo, wt%, bal. Fe) samples of  $7\text{--}9 \times 12 \times 4\text{--}5 \text{ mm}^3$  were ground using SiC P600 grid paper prior to coating application. Then, the enamel ceramic coatings were applied in a two-step process that is described elsewhere [2]. The different oxide compositions of the enamel coatings of the study are described in Table 1. Their purity was higher than 99.9%, according to the

supplier (Sigma-Aldrich). However, for clarity purposes, the samples will be referenced as samples A to G in this work.

**Table 1.** Enamel-producing recipes (wt.%) for ceramic coatings development used in this work.

Oxide	Coating Symbol						
	A	B	C	D	E	F	G
SiO <sub>2</sub>	54.13	51.72	56.80	55.76	63.17	45.11	39.79
Al <sub>2</sub> O <sub>3</sub>	-	-	2.89	-	2.22	-	-
B <sub>2</sub> O <sub>3</sub>	18.10	15.79	7.22	2.02	8.32	15.08	12.14
CaO	-	-	4.34	3.01	2.00	-	-
Na <sub>2</sub> O	13.30	13.80	11.46	10.02	12.33	11.08	10.62
K <sub>2</sub> O	-	1.50	9.18	3.25	1.91	-	1.16
ZnO	-	-	-	-	3.05	-	-
Li <sub>2</sub> O	0.62	1.74	-	5.04	-	0.52	1.34
TiO <sub>2</sub>	6.14	7.53	5.69	1.99	3.05	5.11	5.79
BaO	1.99	2.51	-	-	-	1.66	1.93
ZrO <sub>2</sub>	-	-	-	14.94	-	-	-
F	3.68	2.18	-	1.99	1.85	3.07	1.67
CoO	0.41	0.54	1.21	0.99	1.05	0.34	0.41
MnO	1.02	1.61	0.52	0.43	0.45	0.85	1.24
NiO	0.61	1.08	0.69	0.57	0.60	0.51	0.83
Cr <sub>2</sub> O <sub>3</sub>	-	-	-	-	-	16.67	23.08

One shall note that after the application of the selected enamel on the steel substrate (16Mo3) a firing step at 880 °C for about 20 min was conducted. Visual and microscopic assessment of the surface showed no presence of capillary cracks for the coatings of investigation.

## 2.2. Oxidation in Water Vapor

The oxidation of the different samples was carried out using a Setsys Evo 1750 thermobalance (0.1 µg accuracy, SETARAM, Caluire-et-Cuire, France) under a wet Ar atmosphere containing water vapor at 10 vol.%. The water vapor was created using the Wetsys module (SETARAM, Caluire-et-Cuire, France) and transferred to the bottom of the thermal enclosure of the thermobalance via a heated transfer pipe. To assess the different kinetic behaviors of the samples, the specific mass gain ( $\frac{\Delta m}{S}$ ); where  $\Delta m$  is the mass gain of the sample and  $S$  its surface) was plotted on log-log diagram as a function of the time to retrieve the oxidation parameters described by the law of kinetics of Equation (1):

$$\frac{\Delta m}{S} = k \times t^n \quad (1)$$

where  $k$  and  $n$  correspond to the kinetic parameters that are usually employed to describe and compare the different oxidation regimes in the transient stable period that arrives ahead of any slope change or breakaway. On the one hand, if “ $n$ ” is comprised between 0.9 and 1.1, the oxidation kinetic is described by the simple linear Equation (2):

$$\frac{\Delta m}{S} = k_l \times t \quad (2)$$

where  $k_l$  corresponds to the linear rate constant in  $\text{g}\cdot\text{cm}^{-2}\cdot\text{s}^{-1}$ . On the other hand, if “ $n$ ” is comprised between 0.35 to 0.65 a parabolic law allows the determination of the parabolic rate constant  $k_p$  in is  $\text{g}\cdot\text{cm}^{-4}\cdot\text{s}^{-2}$  following the Equation (3):

$$\frac{\Delta m}{S} = \sqrt{k_p \times t} + A \quad (3)$$

where  $A$  is a constant that depends on the transient period [22].

### 2.3. Characterization

The characterization of the materials before and after testing at high temperatures was conducted by scanning electron microscopy (SEM Quanta 200F, FEI, Hillsboro, OR, USA) in a SCIOS FEI dual-beam apparatus coupled to energy dispersive spectrometry (EDS, FEI, Hillsboro, OR, USA) from EDAX [2]. Secondary and backscattered electron images were taken at different magnifications yet only the most representative are included in this paper. The preparation of the cross-section of the samples included gentle polishing with increasing SiC papers (Struers) and final 1- $\mu\text{m}$  diamond polishing with a Struers suspension following conventional metallographic protocols. The polished cross-sections were finally rinsed with water and ethanol and dried. The crystal phase identification was realized by X-ray diffraction (XRD, BRUKER, Karlsruhe, Germany) in a Bruker AXS D8 Advance using the  $\lambda_{\text{Cu}}$  radiation in symmetric  $\theta$ - $2\theta$  mode. The local phase analyses were made possible with Raman micro-spectrometry (Jobin Yvon LabRam HR800, HORIBA, Tulln, Austria) using a laser of  $\lambda = 632 \text{ nm}$ . The porosity in the coatings before and after the water vapor tests was investigated by image analyses using Image J software (version 1.54b) (see highlighted contours in yellow on cross-section micrographs).

## 3. Results

### 3.1. Coatings

Figure 1 gathers the images of the cross-sections of the enamel coatings as observed in the backscattered electrons mode of the SEM, while Table 2 summarizes the main features. It can be observed that all the coatings homogeneously covered the steel substrate irrespective of their composition and variable thickness. Furthermore, except for the negligible porosity of A and B, all the remaining coatings displayed very tiny bubbles (C, D, F, and G) to small (B and D) and coarse pores (E).

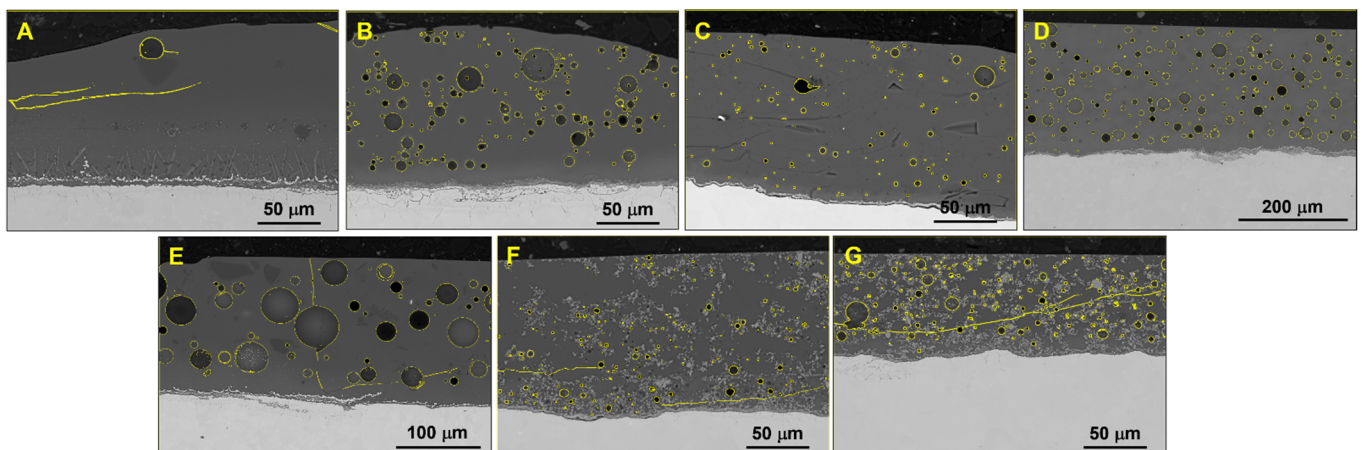


**Figure 1.** SEM cross-section images in the backscattered mode of the glass enamel coatings (coatings (A–G)) in the as-fabricated condition (pores and cracks are highlighted in yellow).

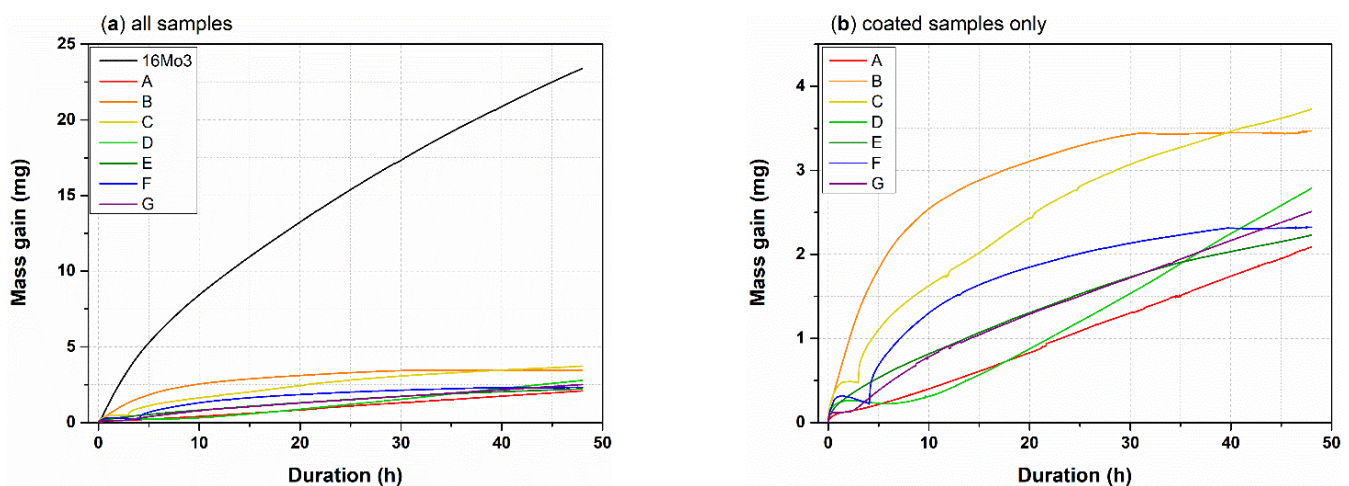
### 3.2. Oxidation in Wet Air

Figure 2 shows the evolution of the specific mass gains of the uncoated and coated steels with time at 650 °C in Ar-10 vol% $\text{H}_2\text{O}$ . It can be noted that the coatings dramatically decreased (8 to 16 times) the mass gain of the uncoated steel (Figure 2a). The coatings themselves evolved very differently upon oxidation (Figure 2b). For instance, a small yet continuous mass uptake occurred with A, but the mass gain of B increased significantly and then slowed down. Other coatings (C, D, and F) tended to exhibit some kind of breakaway oxidation after about 5 h. At the end of the test, the highest mass gain after 48 h of annealing in Ar-10% $\text{H}_2\text{O}$  at 650 °C was reported for C ( $0.85 \text{ mg}\cdot\text{cm}^{-2}$ ) and the lowest mass gain was recorded for ceramic sample A ( $0.42 \text{ mg}\cdot\text{cm}^{-2}$ ). However, the final specific mass gain is not sufficient to describe the oxidation behavior of each specimen. For a better understanding

of the kinetic behavior of each sample, the oxidation parameters ( $k$ ,  $n$ ) retrieved from the kinetic law of Equation (1) were calculated at different time intervals for each specimen that depends on the different transient periods observed and are gathered in Table 3.

**Table 2.** Summary of the main microstructural features of the enamel coatings on low-alloyed 16Mo3 boiler steel (the vol.% of porosity is based on image analyses of the cross-sections and should be considered as comparative values).

	Thickness ( $\mu\text{m}$ )	Porosity (vol.%)	Cracks (Orientation)	Coating-Substrate Interface
A	$100 \pm 25$	1%	Parallel	Oxide and corrosion layer
B	$80 \pm 15$	3%	None	Thin oxide and corrosion layer
C	$110 \pm 25$	14%	None	Continuous thin oxide layer
D	$230 \pm 15$	25%	None	Thin oxide and corrosion layer
E	$170 \pm 20$	34%	Normal and parallel	Thin oxide and corrosion layer
F	$150 \pm 10$	15%	Parallel	Continuous thin oxide layer
G	$90 \pm 5$	18%	Parallel	Continuous thin oxide layer



**Figure 2.** Specific mass gain curves obtained by TGA of (a) the raw material (reference 16Mo3) and coated samples exposed to Ar-10% $\text{H}_2\text{O}$  at 650 °C for 48 h; (b) presents the data of the coated samples only.

As expected from Figure 2, after a linear growth from the onset of oxidation to 4 h, the uncoated 16Mo3 shows fast oxidation kinetics described by a parabolic constant " $k_p$ " of  $3.17 \cdot 10^{-10} \text{ g}^2 \cdot \text{cm}^{-4} \cdot \text{s}^{-1}$  that is approximately two orders of magnitude higher than that the coated samples. The discrepancy in the oxidation behavior of the different coated specimens is evident from the values of Table 3 after an initial short transition period. Indeed, A, D, and G exhibit continuous linear oxidation after 7 h to 13 h, while B, C, E, and F show parabolic oxidation behavior that stabilizes after 4 to 11 h of oxidation. The peculiar breakaway behavior observed in C and F can be related to the appearance of cracks in the coating or in the oxide but without any spallation. The cracks would allow direct access of the substrate to the water vapor provoking an accelerated attack. The B and F samples did not gain further mass after some oxidation period, which could be related to a very protective oxide scale and/or a densification of the coating that prevented further oxidation.

Figure 3 shows the XRD analyses performed on unexposed and exposed samples while Figure 4 and Table 4 show the results of the Raman analyses. The 16Mo3 substrate is covered with a lepidocrocite  $\gamma\text{-FeOOH}$  and goethite  $\text{Fe(III)OOH}$  oxide layer in the as-received conditions that further transforms into hematite  $\alpha\text{-Fe}_2\text{O}_3$  after exposure to 650 °C for 48 h in the Ar-10% $\text{H}_2\text{O}$  atmosphere. In contrast, the Raman spectra do not display any

significant difference between the as-deposited and the oxidized enamel coatings, while the X-ray patterns of Figure 3b indicate the formation of some new phases attributed to the crystallization of silicate compounds.

**Table 3.** Oxidation parameters “n” and “k” of the uncoated and coated samples as a function of different time intervals.

Material	Time Interval; Oxidation Parameters “n” and “k” **,**			
16Mo3	0–1 h transition	1–4 h n = 1: linear * $k_l = 8.12 \cdot 10^{-8}$	4–48 h n = 0.65: parabolic ** $k_p = 3.17 \cdot 10^{-10}$	–
A	0–1 h n = 0.49: parabolic ** $k_p = 1.20 \cdot 10^{-13}$	1–7 h transition	7–48 h n = 1.05: linear * $k_l = 2.51 \cdot 10^{-9}$	–
B	0–20 min n = 0.51: parabolic ** $k_p = 1.20 \cdot 10^{-13}$	20–30 min transition	30 min–7 h n = 0.75: sub-linear * $k_l = 2.32 \cdot 10^{-8}$	7–48 h n = 0.3: ~parabolic ** $k_p = 1.64 \cdot 10^{-12}$
C	0–1 h n = 0.45: parabolic ** $k_p = 2.28 \cdot 10^{-12}$	1–4 h breakaway without spallation	4–48 h n = 0.55: parabolic ** $k_p = 4.80 \cdot 10^{-12}$	–
D	0–10 h transition	10–48 h n = 1.4: super-linear * $k_l = 4.31 \cdot 10^{-9}$	–	–
E	0–30 min transition	30 min–11 h n = 0.55: parabolic ** $k_p = 1.39 \cdot 10^{-12}$	11–48 h n = 0.65: parabolic ** $k_p = 2.66 \cdot 10^{-12}$	–
F	0–30 min n = 0.56: parabolic ** $k_p = 1.69 \cdot 10^{-12}$	30 min–4 h breakaway without spallation	4–40 h n = 0.53: parabolic ** $k_p = 1.66 \cdot 10^{-12}$	40–48 h evaporation
G	0–3 h transition	3–13 h n = 1.2: super-linear * $k_l = 4.37 \cdot 10^{-9}$	13–48 h n = 0.74: linear * $k_l = 2.49 \cdot 10^{-9}$	–

\*  $k_l$ , linear constant of oxidation in  $\text{g} \cdot \text{cm}^{-2} \cdot \text{s}^{-1}$ ; \*\*  $k_p$ , parabolic constant of oxidation in  $\text{g}^2 \cdot \text{cm}^{-4} \cdot \text{s}^{-1}$ .

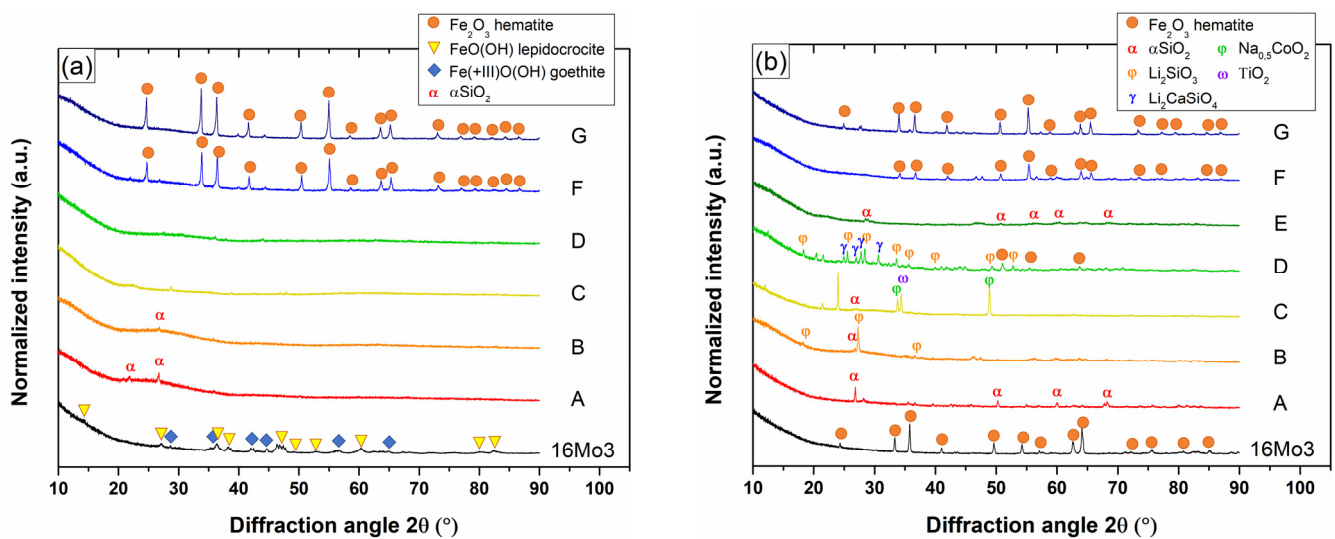


**Figure 3.** XRD diffraction plots for (a) the initial samples and (b) the oxidized samples at 650 °C for 48 h in Ar-10% $\text{H}_2\text{O}$  atmosphere.

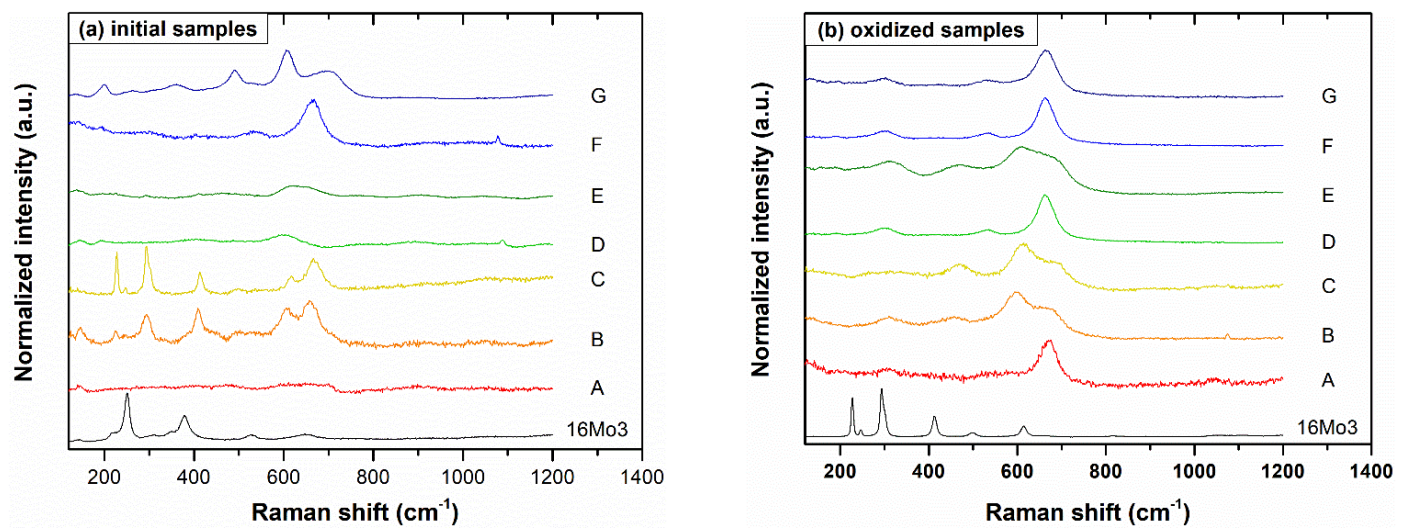


**Figure 4.** Raman spectra for (a) initial and (b) oxidized samples at 650 °C for 48 h in Ar-10% $\text{H}_2\text{O}$  atmosphere.

Figure 5 shows SEM images of the exposed surfaces of the uncoated 16Mo3 steel and the coated samples in an Ar-10% $\text{H}_2\text{O}$  atmosphere for 48 h at 650 °C. For uncoated 16Mo3 (Figure 5A), some cracks as well as two types of microstructures are observed with oxides exhibiting a platelet-like morphology on the external surface and round-shaped oxides underneath that are revealed as spallation occurred. For the coated samples, various microstructures were observed on the surfaces exposed to the Ar-10% $\text{H}_2\text{O}$  atmosphere for 48 h at 650 °C. For A, B, and E, small pores were observed (Figure 5B,C,F). Only D samples exhibited partial spallation of the coating (Figure 5E). This spallation probably occurred upon cooling, as no evidence of spallation was observed during the TGA analysis. In the case of F (Figure 5G), some tiny bright precipitates were observed on top of the coatings, whereas the precipitates observed for the other coatings appeared to be embedded in the silica matrix.

Figure 6 shows the cross-section SEM images of the uncoated and coated 16Mo3 steel exposed to Ar-10% $\text{H}_2\text{O}$  atmosphere at 650 °C for 48 h, while Table 5 summarizes the major features after oxidation compared to the as-fabricated coatings. Irrespective of the coating thickness that may differ from one batch to the other, it is interesting to observe that barely any significant interfacial oxide scale grew between the coating and the substrate. In contrast, the uncoated 16Mo3 developed a very thick (~120  $\mu\text{m}$ ) dual oxide layer separated by a porous interlayer. The upper sublayer contains cracks.

**Table 4.** Raman peaks position and corresponding phases.

Initial Samples:	Peaks Position ( $\text{cm}^{-1}$ )								
	16Mo3	A	B	C	D	E	F	G	G
			~142 <sup>3</sup>						
	~220 <sup>1</sup>		~223 <sup>2</sup>	~228 <sup>2</sup>					~198 <sup>2</sup>
	~250 <sup>1</sup>		~243 <sup>2</sup>	~245 <sup>2</sup>					~264 <sup>2</sup>
	~307 <sup>1</sup>		~295 <sup>2</sup>	~292 <sup>2</sup>			~301 <sup>3</sup>		~359 <sup>2</sup>
	~347 <sup>1</sup>	-	~411 <sup>2</sup>	~412 <sup>2</sup>	-	-	~533 <sup>3</sup>		~431 <sup>2</sup>
	~379 <sup>1</sup>		~500 <sup>2</sup>	~496 <sup>2</sup>			~662 <sup>3</sup>		~536 <sup>3</sup>
	~529 <sup>1</sup>		~535 <sup>3</sup>	~616 <sup>2</sup>					~607 <sup>2</sup>
	~644 <sup>1</sup>		~605 <sup>2</sup>	~667 <sup>3</sup>					~695 <sup>3</sup>
			~660 <sup>3</sup>						

Table 4. Cont.

Oxidized samples:	Peaks Position (cm <sup>-1</sup> )							
	16Mo3	A	B	C	D	E	F	G
~227 <sup>2</sup>								
~248 <sup>2</sup>								
~295 <sup>2</sup>		~308 <sup>3</sup>	~311 <sup>3</sup>	~465 <sup>3</sup>	~304 <sup>3</sup>	~312 <sup>3</sup>	~304 <sup>3</sup>	~304 <sup>3</sup>
~413 <sup>2</sup>		~538 <sup>3</sup>	~460 <sup>3</sup>	~612 <sup>3</sup>	~533 <sup>3</sup>	~467 <sup>3</sup>	~535 <sup>3</sup>	~534 <sup>3</sup>
~500 <sup>2</sup>		~667 <sup>3</sup>	~600 <sup>2</sup>	~682 <sup>3</sup>	~662 <sup>3</sup>	~610 <sup>2</sup>	~664 <sup>3</sup>	~664 <sup>3</sup>
~615 <sup>2</sup>			~674 <sup>3</sup>			~675 <sup>3</sup>		
~658 <sup>2</sup>								

Phases: <sup>1</sup> Lepidocrocite FeO(OH); <sup>2</sup> Hematite Fe<sub>2</sub>O<sub>3</sub>; <sup>3</sup> Magnetite Fe<sub>3</sub>O<sub>4</sub>.

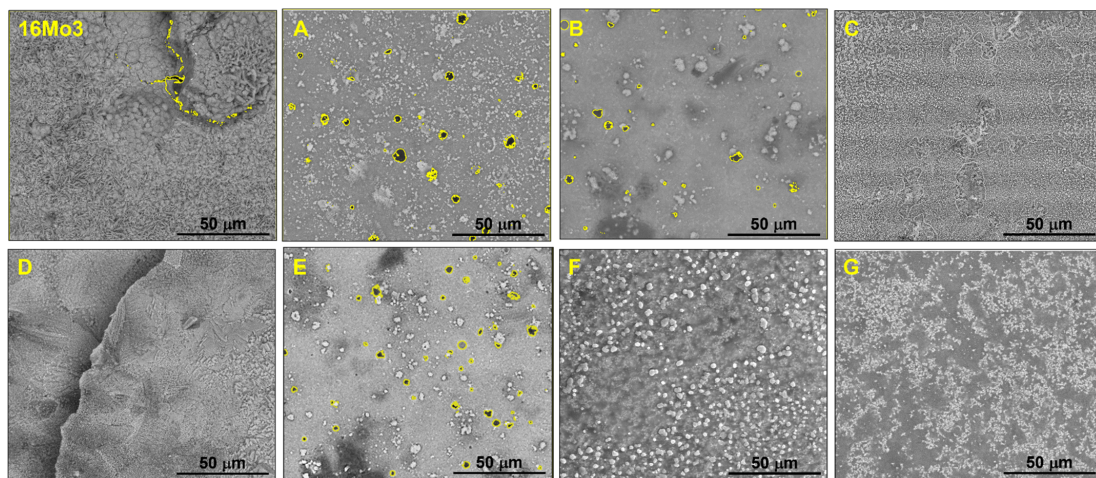


**Figure 5.** SEM images of the surfaces of uncoated 16Mo3 and coated samples ((A–G) coatings) exposed at 650 °C for 48 h in Ar-10%H<sub>2</sub>O atmosphere (pores and cracks are highlighted in yellow). Note that there were no oxide scales formed at the top of the enamel coatings.

In the case of the coatings, it can be noted that the porosity of most coatings did not change with oxidation time and that no cracks were found either. However, the interfacial reaction zone between the coating and the substrate extended while new bright contrasted phases formed at the coating/gas interface. For instance, the porosity of B also vanished, but a significant interfacial reaction similar to that of A before oxidation occurred. The porosity still remained in all other coatings, but interestingly, the cracks mostly disappeared, except in D, which developed significant cracking.

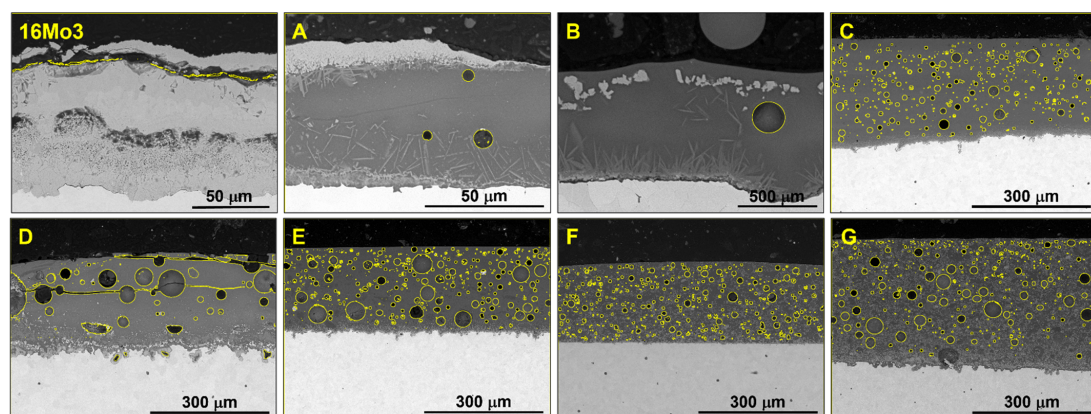


**Figure 6.** SEM images of cross sections of uncoated 16Mo3 and coated samples (A–G) exposed at 650 °C for 48 h in Ar-10%H<sub>2</sub>O atmosphere (pores and cracks are highlighted in yellow).



**Table 5.** Summary of the coating microstructural features of the enamel coatings on low-alloyed 16Mo3 boiler steel after the oxidation at 650 °C for 48 h in wet Ar (the vol.% of porosity is based on image analyses of the cross-sections and should be considered as comparative values). Significant changes compared with the coatings in as-deposited conditions (Table 2) are highlighted using italic font.

	Thickness ( $\mu\text{m}$ )	Porosity (vol.%)	Cracks (Orientation)	Coating-Substrate Interface
A	50–60	2%	Parallel	Thick oxide and corrosion layer
B	30–40	3%	None	Thick oxide and corrosion layer
C	280	14%	None	Thick oxide and corrosion layer
D	110–120	25%	Parallel	Thin oxide and corrosion layer
E	225	34%	None	Thin oxide and corrosion layer
F	200	15%	None	Continuous thin oxide layer
G	300	18%	None	Continuous thin oxide layer

## 4. Discussion

### 4.1. Coatings

In glass enamel coatings like the ones studied here,  $\text{SiO}_2$  and  $\text{B}_2\text{O}_3$  ensure the formation of the network while  $\text{Na}_2\text{O}$ ,  $\text{K}_2\text{O}$ ,  $\text{Li}_2\text{O}$ , and  $\text{CaO}$  are the network modifiers; in particular,  $\text{Li}_2\text{O}$  and  $\text{Na}_2\text{O}$  are strong modifiers. The other oxides provide an intermediate effect, e.g.,  $\text{Al}_2\text{O}_3$  and  $\text{Cr}_2\text{O}_3$  can take part as network formers or modifiers depending on the surrounding environment and coordination with bonding and non-bonding oxygen anions [23]. In this work, the intention was simply to study different chemistries to obtain a variety of coatings that adhere to the substrate. Such adherence results from the corrosion/oxidation of the melt with the steel substrate in all our coatings [24]. Yet, the reactivity of the melt clearly depends on the initial composition of the ceramic frit because either very thin and continuous oxide layers formed (C, D, F, G), a significant interfacial reaction occurred (A), or a mixed situation with corrosion and broken oxide layers (B, E) was observed in Figure 1. The presence of bubbles and porosity in the enamel coatings has been reported in various other works [25] and is ascribed to the gas evolution upon the firing process of the ceramic powder mixture [26]. In contrast, the main differences between the coatings relate to the presence or absence of cracks in the as-fabricated conditions. The cracks mostly depend on the thickness and the thermal expansion coefficients, in particular the latter [27]. This is demonstrated by comparing, e.g., G, which has 90  $\mu\text{m}$  thickness and cracks running parallel to the thickness, with D, whose thickness is more than twice the previous one (230  $\mu\text{m}$ ) but shows no cracking.

### 4.2. Oxidation

The 16Mo3 steel was selected in this work to show the potential efficiency of the ceramic coatings exposed to harsh conditions. The high-temperature oxidation of the steel was already reported in [28]. However, to the best of our knowledge, no study focused on the effects of water vapor that regularly appears in combustion atmospheres. It was anticipated that this poorly alloyed steel will require additional protection with inexpensive coatings like the enamel ones proposed here. This is clearly reflected in Figure 2a, where the uncoated steel underwent a 6-fold increase of mass gain after 48 h of exposure to wet air at 650 °C compared to any of the coatings. Indeed, before oxidation, the uncoated steel is covered with lepidocrocite  $\gamma\text{-FeOOH}$  and goethite  $\alpha\text{-FeOOH}$  despite the initial grinding of the surface of the steel with SiC P600 sandpaper to leave a rust-free surface with a homogeneous roughness. Yet, the kinetics of the formation of lepidocrocite are very fast [29], and it has great thermodynamic stability ( $\Delta H_f^\circ$  (lepidocrocite) =  $-549.4 \pm 1.4 \text{ kJ}\cdot\text{mol}^{-1}$ ) before it transforms into goethite, which is even more stable ( $\Delta H_f^\circ$  =  $-560.7 \pm 1.2 \text{ kJ}\cdot\text{mol}^{-1}$ ) [30]. Lepidocrocite is similar to goethite as they are polymorphs of the same composition with different structures; the lepidocrocite possesses an orthorhombic structure with space group  $A_{\text{mam}}$ . The thermal dehydration of both goethite and lepidocrocite results in the

hematite and maghemite formation by topotactic transformation (oxidation of magnetite to maghemite), where the magnetite phase oxidizes into the maghemite phase by natural weathering or other processes with the conversion of all  $\text{Fe}^{2+}$  ions into  $\text{Fe}^{3+}$  ions [31]. Goethite  $\alpha\text{-FeOOH}$ , lepidocrocite  $\gamma\text{-FeOOH}$ , hematite  $\alpha\text{-Fe}_2\text{O}_3$ , and maghemite  $\gamma\text{-Fe}_2\text{O}_3$  are the constituents of magnetite  $\text{Fe}_3\text{O}_4$  for ferric oxides and oxyhydroxides. Therefore, the oxidation process results in iron vacancies in the crystal lattice due to the partial removal of iron to compensate for the positive charges. The resulting multilayered scale is very similar to the ones observed in other very low-Cr boiler steels such as 13CrMo4 [32] and is believed to arise from the presence of iron vacancies on the FeO scale that foster diffusion, hence provoking the growth of thick oxide layers. As postulated by T. Dudziak, the growth of  $\text{Fe}_2\text{O}_3$  and of  $\text{Fe}_3\text{O}_4$  for which the defects are respectively found in the oxygen sublattice and interstitially (support iron ion diffusion) will sustain further diffusion upon oxidation [33].

In the case of the coatings, different oxidation behaviors have been observed in Figure 2b, but no real surface oxide formation occurs (Figure 5). For instance, only coatings B and F seem to follow a parabolic growth with a sharp oxygen uptake during the first stages and a subsequent transition till the interdiffusion of the cations and oxygen anion through a supposedly single and even oxide scale. Therefore, the oxygen uptake is slowed down with time. In contrast, all the other coatings seem to undergo linear oxidation yet at different rates according to their different slopes. Among the latter, coatings C and D undergo the fastest growth while coatings A and G exhibit the lowest mass gains. Since the TGA curves did not indicate any spallation, the oxidation phenomena can be attributed to either chemical reasons or to the cracking of the coatings. As for the former, it has been noted in Table 1 that the C and D coatings have the lowest amount of  $\text{Na}_2\text{O}$  whereas the best-behaving coatings (B and F) contain the highest  $\text{B}_2\text{O}_3$  concentrations.  $\text{B}_2\text{O}_3$  is known to be a strong glass network former whereas  $\text{Na}_2\text{O}$  has a strong ionic bonding that is easy to break and therefore strongly modifies the Si-O-Si bonds [34]. As a result, the glassy enamel coating loses the relative toughness and develops cracks, as shown in Figure 6 for D. The reasons why C does not crack can be thus related to the greater content of the network stabilizer  $\text{B}_2\text{O}_3$  and of  $\text{K}_2\text{O}$  and  $\text{TiO}_2$ , whose role is to depolymerize the glass and open the network [34]. Yet, the cracks observed in the D coatings run parallel to the gas/coating interface and should not allow the attack of the substrate underneath. Therefore, the increasing mass gain with time shall derive from the very coarse porosity that allows penetration of the water vapor to the coating/substrate interface. This hypothesis is confirmed by paying particular attention to such areas with the presence of pores surrounded by oxides (Figure 6). Such pores can be ascribed to the evaporation of Cr as  $\text{CrO}_2(\text{OH})_{2(\text{g})}$  at  $650\text{ }^\circ\text{C}$ , but there is very little Cr in the steel. Therefore, the presence of oxides in those pores is more likely due to the dissociation of water vapor resulting in  $\text{H}_{2(\text{g})}$  that reduces the iron oxide and fosters the diffusion of metal or cationic iron. Simultaneously, the water vapor can be transported and form oxide around the pores [35]. Therefore, the coatings that underwent densification with the oxidation temperature like coating B underwent the lowest mass gains. It thus derives that glass enamel coatings with sufficiently dense microstructures should be designed to provide a barrier effect against oxidation.

## 5. Conclusions

Different enamel coatings based on  $\text{SiO}_2\text{-Na}_2\text{O-B}_2\text{O}_3\text{-TiO}_2$  oxide phases were investigated as protection for low-alloyed 16Mo3 steel designed for boiler steel in power generation systems. The oxidation in water vapor (Ar + 10 vol.%) at  $650\text{ }^\circ\text{C}$  for 48 h of these coated samples indicates that the ceramic coatings provided a high degree of protection to the steel exposed to such conditions compared to the uncoated 16Mo3 steel. Furthermore, despite the formation of cracks in some coatings, no spallation from the steel surface was observed. As a matter of fact, the enamel displayed a high adherence to the substrate due to a partial dissolution of the substrate by the glass during the elaboration process that led to the bonding of the ceramic to the metal. The extensive attack for coating D was

related to the interconnected porosity in the coating that allowed access of water vapor to the 16Mo3 steel. An accurate assessment of the porosity of the tested coatings should be thus conducted in the future to evaluate such a hypothesis.

**Author Contributions:** Conceptualization, F.P. and T.D.; methodology, F.P. and G.B.; software, G.B.; validation, F.P., T.D., R.T. and E.R.; formal analysis, G.B.; investigation, G.B. and R.T.; resources, E.R. and R.T.; data curation, F.P., G.B. and T.D.; writing—original draft preparation, F.P., G.B. and T.D.; writing—review and editing, F.P. and G.B.; visualization, F.P., G.B. and T.D.; supervision, F.P. and T.D.; project administration, F.P. and T.D.; funding acquisition, F.P., T.D. All authors have read and agreed to the published version of the manuscript.

**Funding:** Part of this work was supported by the Campus France- Nawa Poland exchange program “Polonium” with reference number 46878ZJ. In addition, the work was partly financially supported by Ministry of Higher Education in Poland, in the internal project in Łukasiewicz—Krakow Institute of Technology, under the number: 9011/00.

**Institutional Review Board Statement:** Not applicable.

**Informed Consent Statement:** Not applicable.

**Data Availability Statement:** All data that support the findings of this study are included within the article.

**Acknowledgments:** Part of this work was supported by the Campus France- Nawa Poland exchange program “Polonium” with reference number 46878ZJ. In addition, the work was partly financially supported by Ministry of Higher Education in Poland, in the internal project in Łukasiewicz—Krakow Institute of Technology, under the number: 9011/00.

**Conflicts of Interest:** The authors declare no conflict of interest.

## References

1. Abu-Warda, N.; López, A.J.; Pedraza, F.; Utrilla, M.V. Corrosion Behavior of T24, T92, VM12, and AISI 304 Steels Exposed to KCl–NaCl–K<sub>2</sub>SO<sub>4</sub>–Na<sub>2</sub>SO<sub>4</sub> Salt Mixtures. *Mater. Corros.* **2021**, *72*, 936–950. [[CrossRef](#)]
2. Rząd, E.; Dudziak, T.; Polczyk, T.; Boroń, Ł.; Figiel, P.; Oziębło, A.; Chmielewska, D.; Synowiec, B.; Pichniarczyk, P. Sulfidation of Ceramic-Based Coatings Deposited on Low-Alloyed Steel 16Mo3 Exposed at High Temperature. *J. Mater. Eng. Perform.* **2021**, *30*, 8538–8550. [[CrossRef](#)]
3. Boulesteix, C.; Pedraza, F.; Proy, M.; Lasanta, I.; de Miguel, T.; Illana, A.; Pérez, F.J. Steam Oxidation Resistance of Slurry Aluminum and Aluminum/Silicon Coatings on Steel for Ultrasupercritical Steam Turbines. *Oxid. Met.* **2017**, *87*, 469–479. [[CrossRef](#)]
4. Boulesteix, C.; Kolarik, V.; Pedraza, F. Steam Oxidation of Aluminide Coatings under High Pressure and for Long Exposures. *Corros. Sci.* **2018**, *144*, 328–338. [[CrossRef](#)]
5. Dhand, D.; Kumar, P.; Grewal, J.S. A Review of Thermal Spray Coatings for Protection of Steels from Degradation in Coal Fired Power Plants. *Corros. Rev.* **2021**, *39*, 243–268. [[CrossRef](#)]
6. Kumar, S.; Kumar, M.; Handa, A. Combating Hot Corrosion of Boiler Tubes—A Study. *Eng. Fail. Anal.* **2018**, *94*, 379–395. [[CrossRef](#)]
7. Galetz, M.C.; Bauer, J.T.; Schütze, M.; Noguchi, M.; Cho, H. Resistance of Coatings for Boiler Components of Waste-to-Energy Plants to Salt Melts Containing Copper Compounds. *J. Therm. Spray Technol.* **2013**, *22*, 828–837. [[CrossRef](#)]
8. Jafari, R.; Sadeghimeresht, E.; Farahani, T.S.; Huhtakangas, M.; Markocsan, N.; Joshi, S. KCl-Induced High-Temperature Corrosion Behavior of HVOF-Sprayed Ni-Based Coatings in Ambient Air. *J. Therm. Spray Technol.* **2018**, *27*, 500–511. [[CrossRef](#)]
9. Dudziak, T.; Hussain, T.; Simms, N.J.; Syed, A.U.; Oakey, J.E. Fireside Corrosion Degradation of Ferritic Alloys at 600 °C in Oxy-Fired Conditions. *Corros. Sci.* **2014**, *79*, 184–191. [[CrossRef](#)]
10. Tejero-Martin, D.; Rezvani Rad, M.; McDonald, A.; Hussain, T. Beyond Traditional Coatings: A Review on Thermal-Sprayed Functional and Smart Coatings. *J. Therm. Spray Technol.* **2019**, *28*, 598–644. [[CrossRef](#)]
11. Harrison, W.N.; Moore, D.G.; Richmond, J.C. Ceramic Coatings for High-Temperature Protection of Steel. *J. Res. Natl. Bur. Stand.* **1947**, *38*, 293. [[CrossRef](#)]
12. Pavan, C.M.; Narendra, B.B.R. Review of Ceramic Coating on Mild Steel Methods, Applications and Opportunities. *Int. J. Adv. Sci. Res. Eng.* **2018**, *4*, 44–49. [[CrossRef](#)]
13. Kasala, S.; Vidyavathy, M. Advanced Ceramic Coatings on Stainless Steel: A Review of Research, Methods, Materials, Applications and Opportunities. *Int. J. Adv. Eng. Technol.* **2016**, *7*, 126–141.
14. Adraider, Y.; Pang, Y.X.; Nabhani, F.; Hodgson, S.N.; Sharp, M.C.; Al-Waidh, A. Laser-Induced Deposition of Alumina Ceramic Coating on Stainless Steel from Dry Thin Films for Surface Modification. *Ceram. Int.* **2014**, *40*, 6151–6156. [[CrossRef](#)]

15. Vural, M.; Zeytin, S.; Ucisik, A.H. Plasma-Sprayed Oxide Ceramics on Steel Substrates. *Surf. Coat. Technol.* **1997**, *97*, 347–354. [[CrossRef](#)]
16. Seraffon, M.; Simms, N.J.; Nicholls, J.R.; Sumner, J.; Nunn, J. Performance of Thermal Barrier Coatings in Industrial Gas Turbine Conditions. *Mater. High Temp.* **2011**, *28*, 309–314. [[CrossRef](#)]
17. Sumner, J.; Encinas-Oropesa, A.; Simms, N.J.; Oakey, J.E. High Temperature Oxidation and Corrosion of Gas Turbine Component Materials in Burner Rig Exposures. *Mater. High Temp.* **2011**, *28*, 369–376. [[CrossRef](#)]
18. Peters, M.; Leyens, C.; Schulz, U.; Kaysser, W.A. EB-PVD Thermal Barrier Coatings for Aeroengines and Gas Turbines. *Adv. Eng. Mater.* **2001**, *3*, 193–204. [[CrossRef](#)]
19. Wells, J.; Chapman, N.; Sumner, J.; Walker, P. The Use of APS Thermal Barrier Coatings in Corrosive Environments. *Oxid. Met.* **2017**, *88*, 97–108. [[CrossRef](#)]
20. Ramaswamy, P.; Seetharamu, S.; Rao, K.J.; Varma, K.B.R. Thermal Shock Characteristics of Plasma Sprayed Mullite Coatings. *J. Spray Technol.* **1998**, *7*, 497–504. [[CrossRef](#)]
21. Shen, D.; Li, M.; Gu, W.; Wang, Y.; Xing, G.; Yu, B.; Cao, G.; Nash, P. A Novel Method of Preparation of Metal Ceramic Coatings. *J. Mater. Process. Technol.* **2009**, *209*, 2676–2680. [[CrossRef](#)]
22. Pieraggi, B. Calculations of Parabolic Reaction Rate Constants. *Oxid. Met.* **1987**, *27*, 177–185. [[CrossRef](#)]
23. Schäfer, G. Degradation of Glass Linings and Coatings. In *Shreir's Corrosion*; Elsevier: Amsterdam, The Netherlands, 2010; Volume 3, pp. 2319–2329. ISBN 978-0-444-52787-5.
24. Berdzenishvili, I.G. Functional Corrosion-Resistant Enamel Coatings and Their Adherence Strength. *Acta Phys. Pol. A* **2012**, *121*, 178–180. [[CrossRef](#)]
25. Chen, M.; Li, W.; Shen, M.; Zhu, S.; Wang, F. Glass Coatings on Stainless Steels for High-Temperature Oxidation Protection: Mechanisms. *Corros. Sci.* **2014**, *82*, 316–327. [[CrossRef](#)]
26. Rossi, S.; Russo, F.; Calovi, M. Durability of Vitreous Enamel Coatings and Their Resistance to Abrasion, Chemicals, and Corrosion: A Review. *J. Coat. Technol. Res.* **2021**, *18*, 39–52. [[CrossRef](#)]
27. Son, Y.-K.; Lee, K.H.; Yang, K.-S.; Ko, D.-C.; Kim, B.-M. Prediction of Residual Stress and Deformation of Enamelled Steel. *Int. J. Precis. Eng. Manuf.* **2015**, *16*, 1647–1653. [[CrossRef](#)]
28. Dudziak, T.; Jura, K. High Temperature Corrosion of Low Alloyed Steel in Air and Salt Mist Atmospheres. *Trans. Foundry Res. Inst.* **2016**, *56*, 77–85. [[CrossRef](#)]
29. Xiao, K.; Dong, C.; Li, X.; Wang, F. Corrosion Products and Formation Mechanism during Initial Stage of Atmospheric Corrosion of Carbon Steel. *J. Iron Steel Resist. Int.* **2008**, *15*, 42–48. [[CrossRef](#)]
30. Majzlan, J.; Grevel, K.-D.; Navrotsky, A. Thermodynamics of Fe Oxides: Part II. Enthalpies of Formation and Relative Stability of Goethite ( $\alpha$ -FeOOH), Lepidocrocite ( $\gamma$ -FeOOH), and Maghemite ( $\gamma$ -Fe<sub>2</sub>O<sub>3</sub>). *Am. Mineral.* **2003**, *88*, 855–859. [[CrossRef](#)]
31. Kinebuchi, I.; Kyono, A. Study on Magnetite Oxidation Using Synchrotron X-Ray Diffraction and X-Ray Absorption Spectroscopy: Vacancy Ordering Transition in Maghemite ( $\gamma$ -Fe<sub>2</sub>O<sub>3</sub>). *J. Mineral. Petrol. Sci.* **2021**, *116*, 211–219. [[CrossRef](#)]
32. Pérez, F.J.; Otero, E.; Hierro, M.P.; Gómez, C.; Pedraza, F.; de Segovia, J.L.; Román, E. Corrosion Protection of 13CrMo 44 Heat-Resistant Ferritic Steel by Silicon and Cerium Ion Implantation for High-Temperature Applications. *Surf. Coat. Technol.* **1998**, *108–109*, 121–126. [[CrossRef](#)]
33. Dudziak, T. *Steam Oxidation of Fe-Based Materials High Temperature Corrosion*; Ahmad, Z., Ed.; IntechOpen: London, UK, 2016; pp. 1–25, ISBN 978-953-51-4727-5.
34. Mysen, B.O.; Richet, P. *Silicate Glasses and Melts: Properties and Structure*; Elsevier: Paris, France, 2005; Volume 10.
35. Saunders, S.R.J.; Monteiro, M.; Rizzo, F. The Oxidation Behaviour of Metals and Alloys at High Temperatures in Atmospheres Containing Water Vapour: A Review. *Prog. Mater. Sci.* **2008**, *53*, 775–837. [[CrossRef](#)]

**Disclaimer/Publisher's Note:** The statements, opinions and data contained in all publications are solely those of the individual author(s) and contributor(s) and not of MDPI and/or the editor(s). MDPI and/or the editor(s) disclaim responsibility for any injury to people or property resulting from any ideas, methods, instructions or products referred to in the content.